

Topological Gyromorphs

Laura Gómez Paz^{1,*}, Justin Schirmann^{1,†}, Adam Yanis Chaou^{2,3}, Isidora Araya Day^{2,4,5,‡} and Adolfo G. Grushin^{1,2,6,§}

¹Université Grenoble Alpes, CNRS, Grenoble INP, Institut Néel, 38000 Grenoble, France

²Donostia International Physics Center, P. Manuel de Lardizabal 4, 20018 Donostia-San Sebastian, Spain

³Dahlem Center for Complex Quantum Systems and Fachbereich Physik, Freie Universität Berlin, 14195 Berlin, Germany

⁴QuTech, Delft University of Technology, Delft 2600 GA, The Netherlands

⁵Kavli Institute of Nanoscience, Delft University of Technology, 2600 GA Delft, The Netherlands

⁶IKERBASQUE, Basque Foundation for Science, Maria Diaz de Haro 3, 48013 Bilbao, Spain

(Dated: March 3, 2026)

Gyromorphs are a new class of disordered systems that combine an amorphous-like absence of translational order with quasi-long-range rotational order. Gyromorphs can outperform quasicrystals or hyperuniform arrangements in forming isotropic band gaps, suggesting an avenue to realize robust disordered topological phases. However, gyromorphs lack exact rotational symmetry, which is only realized on average, posing an obstacle for existing real-space invariants to correctly diagnose topological gyromorphs. In this work we show that gyromorphs can host higher-order topological insulating (HOTI) phases protected by average rotational symmetry, and we develop and systematically compare tools for diagnosing topological phases protected by such symmetry. We introduce symmetry indicators of the effective Hamiltonian based on average rotational symmetries which, when combined with the spectral localizer and a scattering invariant, draw a consistent topological phase diagram. Our work unlocks gyromorphs as a novel platform to study topological phases beyond crystals, quasicrystals, and amorphous materials.

Introduction – In the absence of perfect crystalline order, it is still useful to group solids by the action of symmetries on their atomic arrangement. For example, quasicrystals break translational symmetry while retaining long-range order and rotational symmetries, displaying sharp aperiodic diffraction peaks in their structure factor [1, 2]. In contrast, amorphous solids break translational symmetry retaining short-range atomic, which smears out diffraction peaks into well-defined rings [3].

In a recent Letter, Casiulis *et al.* proposed a new class of disorder materials called Gyromorphs [4]. Gyromorphs fill the gap between amorphous and quasicrystalline materials by retaining long-range *discrete* rotational order, as quasicrystals, but disposing of long-range radial order, as amorphous systems. Gyromorphs are the Fourier duals of quasicrystals; the real-space radial distribution function of a gyromorph matches the reciprocal-space features of the structure factor of a quasicrystal, and viceversa [4]. Gyromorphs display average local and average global rotational symmetries, as illustrated in Fig. 1 with a C_8 -symmetric gyromorph (a) and its sharp diffraction peaks (b).

The average rotational symmetries inherent to gyromorphs force us to revisit how we diagnose non-crystalline topological phases. Existing real-space topological methods [5–35] diagnose topological phases in amorphous [15, 16, 36–60] and quasicrystalline [14, 50, 61–79] systems when they are protected by exact on-site and spatial symmetries (e.g., time-reversal, particle-hole, and chiral symmetries). However, for disordered systems with average spatial symmetries, computing a real-space invariant requires imposing global spatial symmetry of a single realization [35, 80, 81], restoring the symmetry via an ensemble of realizations [46, 81, 82], or considering models with exact local spatial symmetry [15, 16, 49, 50]. All these spatial symmetries are absent in a gyromorph.

This methodological limitation leaves topological gyromorphs unclassified, thereby restricting experiments that could

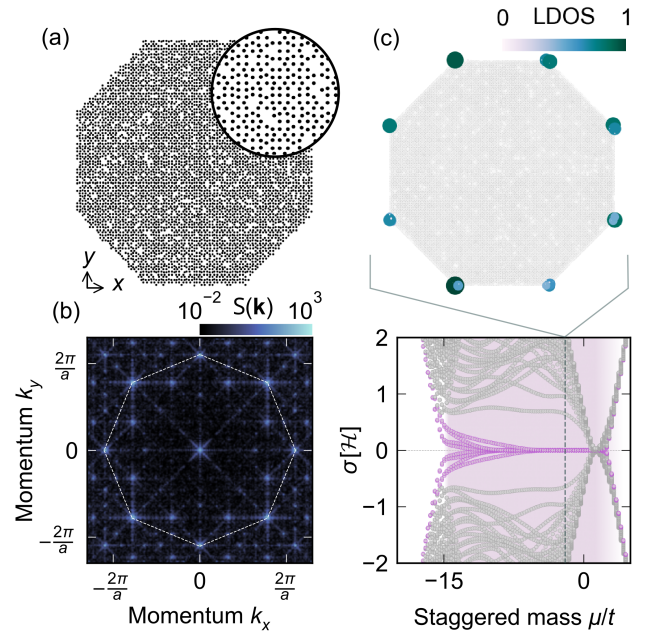


FIG. 1. (a) Real-space representation of the C_8 locally symmetric gyromorph lattice with $N = 5 \times 10^3$ sites. (b) Reciprocal-space structure factor of the gyromorph lattice with $N = 10^4$. The momentum axes are expressed in units of the average lattice spacing $a = 1/\sqrt{N}$. (c) Bottom: 100 smallest eigenvalues of the real-space Hamiltonian Eq. (1), defined on the same lattice as in (b), as a function of the on-site parameter μ . Violet and gray points denote corner and bulk states, respectively. Shading indicates the putative topological region. Top: The local density of states (LDOS) of the zero-energy modes is shown for $\mu/t = -2$.

benefit from their advantageous properties. For example, gyromorphs are able to outperform quasicrystals and hyperuniform

systems in forming clean isotropic spectral gaps [4], an advantageous property for photonic applications [83], and to enhance topological robustness compared to other disordered media. Moreover, naturally grown amorphous materials are in general isotropic, realizing C_∞ symmetry on average [46, 52, 82], and hence are not ideal candidates to host non-crystalline higher-order topological phases [43, 81]. In contrast, gyromorphs have average discrete rotational symmetry C_n built in locally in a single realization, and show well developed spectral gaps without trivially localized in-gap states, features we exploit in this work.

In this work, we demonstrate that gyromorphs host higher-order topological phases and solve the problem of how to identify them. We consider a Hamiltonian on the gyromorph shown in Fig. 1 with local C_8 , particle-hole and time-reversal symmetries and demonstrate that it hosts a higher-order topological phase with eight corner modes. We introduce symmetry indicators of the effective Hamiltonian based on average rotational symmetries. By combining them with spectral localizer and a scattering invariants [35, 84], we establish a consistent topological phase diagram.

Gyromorph tight-binding model – To construct the gyromorph we generate a point set with average local rotation symmetry using the Fast Reciprocal-Space Correlator (FReSCo) [85], an optimization-based method that enforces prescribed features in the point-set’s structure factor. We run the optimization with a set of N uniformly distributed points in two dimensions and impose n rotationally symmetric Bragg peaks in the structure factor at a fixed radial distance $2\pi/a$ from the Γ point, with $a = 1/\sqrt{N}$. We then select an octagonal region from the resulting point set, as depicted in Fig. 1(a). Its structure factor is shown in Fig. 1(b).

On the gyromorph point-set we use the same real space Hamiltonian as in Ref. [68], a pair of oppositely spin-polarized topological superconductors, each in class D,

$$\mathcal{H} = \sum_j \mathbf{c}_j^\dagger \epsilon_j \mathbf{c}_j + \sum_{j,k} f(r_{jk}) \mathbf{c}_j^\dagger T_{jk} \mathbf{c}_k, \quad (1)$$

with $\mathbf{c}_j^\dagger = (c_{j\uparrow}^\dagger, c_{j\downarrow}^\dagger, c_{j\downarrow}, c_{j\uparrow})$, $c_{j,\sigma}^\dagger$ the creation operator at site j with spin \uparrow, \downarrow , ϵ_j the on-site potential, T_{jk} the all-to-all hopping matrix, and $f(r_{jk})$ the hopping strengths as a function of the inter-atomic distances $r_{jk} = |\mathbf{r}_j - \mathbf{r}_k|$. The Pauli matrices σ and τ act on the spin and electron-hole degrees of freedom, respectively. To ensure that the model respects the average local C_n symmetry of the gyromorph point-set we use the model in Ref. [68] for a second-order two-dimensional topological insulator [86–93]

$$T_{jk} = \frac{t}{2} \sigma_z \otimes (\tau_z - i [\tau_x \cos(\theta_{jk}) + \tau_y \sin(\theta_{jk})]) + \frac{V}{2} \cos\left(\frac{n}{2} \theta_{jk}\right) \sigma_y \otimes \tau_0, \quad (2)$$

$$\epsilon_j = \mu (\sigma_z \otimes \tau_z), \quad (3)$$

where t is the hopping strength [94], μ is a staggered mass potential, θ_{jk} corresponds to the bond angle between the site j

and the site k , and V couples opposite spins. Additionally, to ensure a local Hamiltonian we choose $f(r_{jk})$ to decay exponentially with the separation between sites r_{jk} [36]

$$f(r_{jk}) = \exp(1 - r_{jk}/R) \Theta(R - r_{jk}), \quad (4)$$

where R is the cutoff for the hoppings with a value proportional to $1/\sqrt{N}$ and Θ is the Heaviside function. The Hamiltonian in Ref. [68] is composed of two spin-polarized layers and preserves $C_n M$

$$C_n = \exp\left(-i \frac{\pi}{n} \sigma_0 \otimes \tau_z\right), \quad (5a)$$

$$M = \sigma_z \otimes \tau_0, \quad (5b)$$

where C_n is an n -fold rotation within a layer and M is a mirror operator that maps one layer to the other. The last term in (2) forces n to be a multiple of four; we fix $n = 8$ in what follows. The gyromorphic Hamiltonian, therefore satisfies average $C_8 M$ symmetry and exact particle-hole ($\mathcal{P}^2 = +1$), time-reversal ($\mathcal{T}^2 = +1$) and chiral symmetries, placing it in class BDI. The symmetry’s representations are detailed in Appendix A.

Figure 1(c) shows the energy spectrum for the gyromorph Hamiltonian as a function of μ . For values of parameters $t = 1$, $V = 2$, $R = 2.265a$, and $N = 10^4$, we observe a range of μ for which there are eight in-gap states localized at the corners of the octagonal sample, as shown in the top panel. Away from two gap closings transitions at $\mu \sim -15$ and $\mu \sim 2$, the spectrum (excluding corner states) retains a clean gap. This contrasts findings in similar models of amorphous systems, where the spectral gaps close because of disorder [43, 81]. This advantageous feature, seen in photonic gyromorphs [4], results in well-defined bulk-gaps in the electronic spectrum, seen in Fig. 1.

Average symmetry indicators – Our next goal is to establish if the in-gap corner modes are topologically protected. To do so we develop a symmetry indicator that explicitly uses the average C_8 symmetry of the gyromorph. Our approach is based on a momentum-space effective Hamiltonian [68] which has already shown promise to diagnose topology in amorphous systems [4, 15, 49]. It is defined as

$$H_{\text{eff}}(\mathbf{k}) = \frac{1}{2} (G_{\text{eff}}^{-1}(\mathbf{k}) + [G_{\text{eff}}^{-1}(\mathbf{k})]^\dagger). \quad (6)$$

where $G_{\text{eff}}(\mathbf{k})_{l,l'} = \langle \mathbf{k}, l | G | \mathbf{k}, l' \rangle$ is the zero-energy Green’s function $G = \lim_{\eta \rightarrow 0} (\mathcal{H} + i\eta)^{-1}$ projected onto normalized plane-waves $|\mathbf{k}, l\rangle$ for each momentum \mathbf{k} and orbital l . Based on the effective Hamiltonian [68], Refs. [15, 16, 49] developed symmetry indicators for spatial symmetries (including rotations) that are locally exact.

One advantage of the effective Hamiltonian is that it has a ‘disorder averaging’ effect in the thermodynamic limit, restoring average (local) symmetries of the system to exact symmetries of H_{eff} . This enables the identification of topological phases using symmetry eigenvalues of $C_8 M$ at high-symmetry momenta. The absence of translation symmetry in gyromorphs

poses a new problem: at which momenta should one look for band inversions? The lack of a reciprocal lattice prevents us from identifying high-symmetry points at the edge of the Brillouin zone. We observe that we may still use the C_8M operator to find the momenta that minimize the norm of $[H_{\text{eff}}(\mathbf{k}), C_8M]$ thus revealing the effective high-symmetry-like momenta.

Fig. 2(a) shows the norm of said commutator over a range of momenta, and Fig. 2(b) shows the minimal gap Δ of $H_{\text{eff}}(\mathbf{k})$ for all values of μ . Strikingly, we observe that the effective Hamiltonian's gap only closes at the high-symmetry-like momenta $\Gamma = (0, 0)$ and A , Points related to A by C_8 carry no additional information. Gap closings also occur at high-symmetry momenta with $|\mathbf{k}| > 2\pi/a$, but as the disorder-induced self energy becomes increasingly important at momenta beyond $|\mathbf{k}| \sim 2\pi/a$, predictions based off $H_{\text{eff}}(\mathbf{k})$ become unreliable [82]. Hence we do not consider them in the symmetry analysis.

Based on these considerations we construct the average symmetry indicators focusing on $H_{\text{eff}}(\Gamma)$ and $H_{\text{eff}}(A)$. At these points, validated by Fig. 2(a), we can label the Hamiltonian bands by C_8M eigenvalues for different values of μ/t , as shown in Fig. 2(c). The bulk-gap closings for these momenta Fig. 2(b) happen at values of μ/t close to where the spectrum of the real-space Hamiltonian in Fig. 1(c) is gapless. We observe symmetry eigenvalue inversions as a function of μ/t , at Γ for $\mu/t \sim -15$ and at A for $\mu/t \sim 2.5$; signaling topological phase transitions at both gap closing points [95–98].

Real-space invariants – The inversion of symmetry eigenvalues of H_{eff} confirm that the phase within $-15 < \mu/t < -2.5$ and outside this interval are topologically distinct phases of matter. To unequivocally demonstrate a higher-order topological phase what remains is to apply real-space invariants that probe local symmetries, because higher-order topological insulators in $2d$ require either particle-hole or chiral symmetries to protect corner modes. We demonstrate that the gyromorph may realize either higher-order topological phases by applying existing but complementary approaches: a symmetry-reduced spectral localizer [28, 29] and a scattering invariant [35]. We choose the former to diagnose a chiral-symmetry protected phase, and the latter to diagnose a phase protected by particle-hole and eight-fold rotation symmetry [99].

The spectral localizer [8, 29] is a real-space operator whose spectral properties enable the formulation of topological invariants by quantifying how far the position and Hamiltonian operators are from commuting. Besides discrete symmetries, the localizer formalism allows to treat crystalline symmetries like mirror or inversion symmetries [28]. However, it is currently not possible to deal with rotational symmetry in the same way, and only serves as a probe for *extrinsic* higher-order phases [91, 100], further motivating the necessity of the symmetry indicator approach we developed in Fig. 2.

Nevertheless, we may still use the localizer formalism to diagnose topology stemming from discrete symmetries of Eq. (1), in our case an anticommuting chiral operator $\mathcal{S} = \mathbb{1}_N \otimes \sigma_x \otimes \tau_0$.

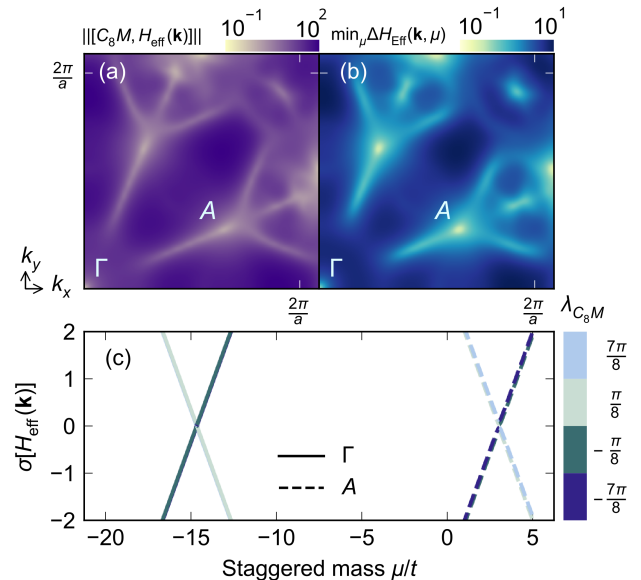


FIG. 2. (a) Norm of the commutator $[H_{\text{eff}}(\mathbf{k}), C_8M]$ from Eqs. (5) and (6) in momentum space. (b) Minimum bulk gap of the effective Hamiltonian in momentum space for $\mu/t \in [-20, 5]$, in logarithmic scale. The points Γ and A correspond to the high-symmetry momenta where the bulk gap closes. (c) Spectrum of the effective Hamiltonian computed at the Γ and A points represented by solid and dashed lines, respectively, as a function of the mass parameter μ/t . The color encodes the C_8M eigenvalues associated with each subspace. We see two crossings as a function of μ/t , each involving a different pair of symmetry eigenvalues.

To this end we use the symmetry-reduced spectral localizer [28]

$$\tilde{L}_{\mathbf{x}} = [i\mathcal{H} + \kappa \hat{e}_d \cdot (\mathbf{X} - \mathbf{x}\mathbb{1})]\mathcal{S}, \quad (7)$$

which chooses a combination of position operators $\mathbf{X} = (X, Y)$ along the direction of the unit vector \hat{e}_d , κ as a tuning parameter that ensures consistent units, $\mathbb{1}$ is shorthand notation for $\mathbb{1}_N \otimes \sigma_0 \otimes \tau_0$, and \mathbf{x} as the position to compute the localizer.

We can use Eq. (7) to signal topological phase transitions through its half-signature

$$\zeta_{\mathbf{x}} = \frac{1}{2} \text{sig}(\tilde{L}_{\mathbf{x}}), \quad (8)$$

defined as the half-difference between positive and negative eigenvalues. To demonstrate how, we ask what is the action of $\tilde{L}_{\mathbf{x}}$ on a spatially localized zero-mode of \mathcal{H} , such as potential corner-modes. By definition, the first term in Eq. (7) acts trivially on a zero-mode of \mathcal{H} . The second term, for small κ , shifts the zero mode slightly up or down from zero, depending on whether the zero mode has positive or negative chirality, and whether it is positioned to the left or right of the chosen \mathbf{x} along \hat{e}_d . Hence, as we tune \mathbf{x} we will match the projected position of a corner state along \hat{e}_d , and a localizer eigenvalue will cross zero, changing the localizer's half-signature.

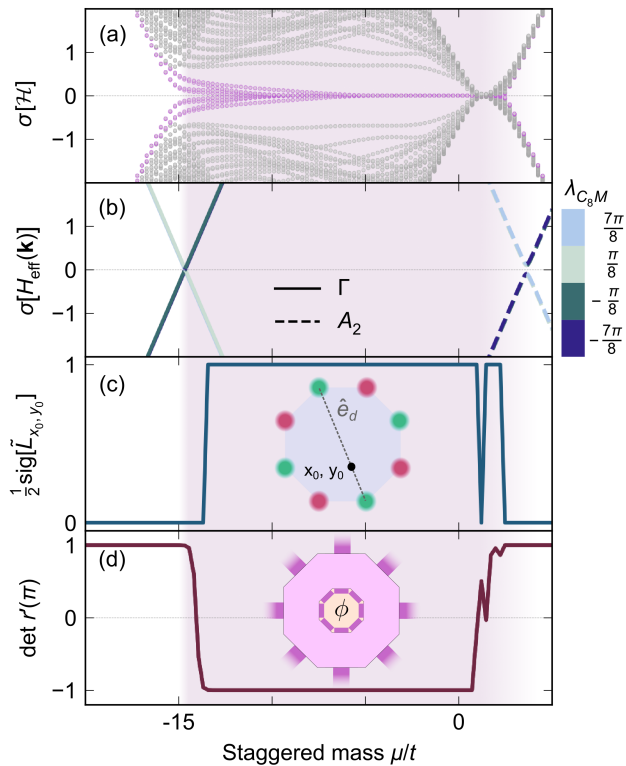


FIG. 3. Topological phase diagram as a function of the staggered mass μ/t . (a) Real-space Hamiltonian spectrum from Fig. 1(c). (b) Inversion of the C_8M eigenvalues at the gap closings of the effective Hamiltonian at the high-symmetry momenta from Fig. 2 (c) Half-signature of symmetry reduced localizer from Eq. (8) for $\kappa = 0.5$, and $\mathbf{x} = (x_0, y_0)$ shown in the inset. Green and red circles denote the positive and negative chiral charges of the corner modes. The numerical instability at $\mu/t \sim 0$ is consistent with a small gap of both the Hamiltonian and spectral localizer, see Appendix B. (d) Higher-order scattering invariant from Eq. (11), computed using the eight-fold symmetric transport setup shown in the inset.

This implies that the half-signature counts the net chiral charge of zero-energy modes projected onto the direction along \hat{e}_d at the specific location \mathbf{x} (see Section B and Refs. [28, 29]). By choosing \hat{e}_d along a direction connecting two opposite vertices of the octagon and $\mathbf{x} = (x_0, y_0)$ on that line, as depicted in the inset of Fig. 3(c), we can then signal a topological transition. This expectation is confirmed by Fig. 3(c) that shows Eq. (8) changing at the values of μ/t matching those where there is a Hamiltonian bulk-gap closing, shown in Fig. 3(a), and when the C_8 symmetry eigenvalues invert, shown in Fig. 3(b).

As an additional confirmation of the topological phase diagram of the gyromorph, we use the scattering theory of higher-order topological phases [35]. In contrast to the localizer, this has the added advantage that it directly probes bulk topology and thus identifies *intrinsic* higher-order phases rather than just extrinsic ones. Differently from the spectral localizer and the effective Hamiltonian, the scattering invariant does not probe bulk-gap closings, but rather delocalization transitions of the

bulk states at the Fermi level by using a transport setup [84]. This probe, however, requires the exact symmetries of the Hamiltonian to hold in order to constrain the scattering equations, so we enforce an additional global C_8M symmetry of the system. Nevertheless, introducing such exact global symmetry retains the average local symmetries that protect the bulk topology [80].

We thus construct the scattering setup by considering a $1/8$ -slice of the gyromorph model and applying C_8M . We remove all sites inside a radius from the center of the sample, and attach a pair of C_8M -symmetric leads to the inner and outer radius of the sample. Then we thread a flux ϕ through the hole and compute the reflection matrix $r(\phi)$ from the inner lead.

The topological invariant follows from the procedure developed in Ref. [35] and we briefly summarize it here. We start by constraining the reflection matrix using the particle-hole \mathcal{P} and C_8M symmetries of the Hamiltonian:

$$C_8M : r(\phi) = Q_{C_8M} r(\phi) V_{C_8M}^\dagger \quad (9)$$

$$\mathcal{P} : r(\phi) = r^*(-\phi), \quad (10)$$

where Q_{C_8M} and V_{C_8M} are matrices that act on the incoming and outgoing modes, respectively. The first constraint allows us to block-diagonalize the reflection matrix into eight blocks, while the second constraint allows us to make $r(\phi)$ real at $\phi = 0, \pi$. At $\phi = \pi$, the ± 1 subspaces of the C_8M operator commute with particle-hole symmetry, allowing us to define

$$\nu = \det r'(\pi), \quad (11)$$

where r' is a real block of the reflection matrix corresponding to the $+1$ eigenvalue of C_8M . Additionally, because a gapped sample must have a unitary reflection matrix, Eq. (11) may only take values ± 1 : $\nu = -1$ signals a topological phase, while $\nu = 1$ corresponds to a trivial phase. Similarly to a Hamiltonian invariant, the only way to change the value of ν is by undergoing a delocalization transition of the bulk states at the Fermi level or by breaking the symmetries that constrain the scattering equations. Fig. 3(d) shows the result as a function of μ/t , whose transitions agree with the rest of Fig. 3.

Conclusions – Gyromorph’s ability to retain well-defined gaps with topological corner modes while being intrinsically disordered suggests that they are a promising platform to realize robust non-crystalline higher-order topological phases. We were able to demonstrate a topological higher-order topological phase in a gyromorph despite them lacking global rotational symmetry. To do so, we have developed symmetry indicators based only on average local rotational symmetry, labeling the topological phase transition with average C_8 eigenvalues. Then we used the spectral localizer and scattering invariants to confirm the higher-order topological phase, as this phase requires an additional chiral or particle-hole symmetry. Taken together our combined methodology correctly diagnoses higher-order topological phases protected by gyromorphic average local rotational symmetry. With this development gyromorphs now exist as a novel class of disordered materials that can host robust topological phases.

Topological photonic systems [63, 101] are a natural platform to explore and take advantage of topological gyromorphs, as this is the context where they were proposed [4], and higher-order topology has been experimentally realized [102]. Other platforms, like CO molecules on metallic surfaces, have already realized higher order phases without crystalline symmetry, and might be appropriate to realize topological gyromorphs [103]. We have restricted ourselves to two-dimensional gyromorphs but they exist in three-dimensions [4], as do photonic realizations of higher-order topological insulators [104]. In conjunction with our work, these may allow the design of electromagnetic wave propagation in disordered media with well defined band-gaps [83]. Exploring topological gyromorphs along these directions is an interesting avenue for future work.

Acknowledgments – We thank A. Cerjan and C. Fulga for insightful discussions about the spectral localizer, and A. R. Akhmerov and D. Varjas for help on algorithmic optimizations. We also thank A. R. Akhmerov for useful discussions about the scattering invariant. All authors are supported by the European Research Council (ERC) Consolidator grant under grant agreement No. 101042707 (TOPOMORPH). A. Y. C. acknowledges financial support from the Deutsche Forschungsgemeinschaft (DFG, German Research Foundation), project number 277101999, CRC TR 183 (projects A03). I. A. D. acknowledges financial support from the Netherlands Organization for Scientific Research (NWO/OCW) as part of the Frontiers of Nanoscience program.

Code availability – The codes and data to reproduce the figures in this work can be found in Ref. [105]. Numerical calculations were performed using the Kwant code [106]

* laura.gomez-paz@neel.cnrs.fr
 † justin.schirmann@gmail.com
 ‡ isidora@araya.day
 § grushin@dipc.org

- [1] D. Shechtman, I. Blech, D. Gratias, and J. W. Cahn, *Phys. Rev. Lett.* **53**, 1951 (1984).
- [2] T. Janssen, G. Chapuis, and M. d. Boissieu, *Aperiodic Crystals From Modulated Phases to Quasicrystals*, Acta Crystallographica Section A, Vol. 74 (Oxford University Press, 2018).
- [3] R. Zallen, *The Physics of Amorphous Solids* (John Wiley & Sons, Ltd, 1998).
- [4] M. Casiulis, A. Shih, and S. Martiniani, *Phys. Rev. Lett.* **135** (2025).
- [5] A. Kitaev, *Ann. Phys.* **321**, 2 (2006), january Special Issue.
- [6] D. Ceresoli and R. Resta, *Phys. Rev. B* **76**, 012405 (2007), publisher: American Physical Society.
- [7] R. Bianco and R. Resta, *Phys. Rev. B* **84**, 241106 (2011).
- [8] T. A. Loring and M. B. Hastings, *EPL* **92**, 67004 (2010).
- [9] E. Prodan, *New J. Phys.* **12**, 065003 (2010).
- [10] E. Prodan, *J. Phys. A* **44**, 113001 (2011).
- [11] A. Marrazzo and R. Resta, *Phys. Rev. B* **95**, 121114 (2017), publisher: American Physical Society.
- [12] T. A. Loring, *Ann. Physics* **356**, 383 (2015).
- [13] Y. Akagi, H. Katsura, and T. Koma, *J. Phys. Soc. Japan* **86**, 123710 (2017), 1709.05853.
- [14] T. A. Loring, [arXiv:1907.11791](https://arxiv.org/abs/1907.11791) (2019).
- [15] Q. Marsal, D. Varjas, and A. G. Grushin, *Proc. Natl. Acad. Sci.* **117**, 30260 (2020).
- [16] P. Corbae, S. Ciocys, D. Varjas, E. Kennedy, S. Zeltmann, M. Molina-Ruiz, S. M. Griffin, C. Jozwiak, Z. Chen, L.-W. Wang, A. M. Minor, M. Scott, A. G. Grushin, A. Lanzara, and F. Hellman, *Nat. Mater.* **22**, 200 (2023).
- [17] A. A. Markov and A. N. Rubtsov, *Phys. Rev. B* **104**, L081105 (2021).
- [18] H. Schulz-Baldes and T. Stoiber, *Europhys. Lett.* **136**, 27001 (2022).
- [19] J. D. Hannukainen, M. F. Martínez, J. H. Bardarson, and T. K. Kvornning, *Phys. Rev. Lett.* **129**, 277601 (2022).
- [20] P. d’Ornellas, R. Barnett, and D. K. K. Lee, *Phys. Rev. B* **106**, 155124 (2022).
- [21] D. Mu textasciitilde noz Segovia, P. Corbae, D. Varjas, F. Hellman, S. M. Griffin, and A. G. Grushin, *Phys. Rev. Res.* **5**, L042011 (2023).
- [22] L. Jezequel and P. Delplace, *SciPost Phys.* **17**, 060 (2024).
- [23] R. Favata and A. Marrazzo, *Electron. Struct.* **5**, 014005 (2023).
- [24] H. Schulz-Baldes, [arXiv:2403.18948](https://arxiv.org/abs/2403.18948) (2024).
- [25] S. Franca and A. G. Grushin, *Phys. Rev. B* **109**, 195107 (2024).
- [26] J. D. Hannukainen, M. F. Martínez, J. H. Bardarson, and T. K. Kvornning, *Phys. Rev. Res.* **6**, L032045 (2024).
- [27] A. J. Uría-Álvarez, D. Molpeceres-Mingo, and J. J. Palacios, *Phys. Rev. B* **105**, 155128 (2022).
- [28] A. Cerjan, T. A. Loring, and H. Schulz-Baldes, *Phys. Rev. Lett.* **132** (2024).
- [29] A. Cerjan and T. A. Loring, *APL Photonics* **9** (2024).
- [30] D. Li, C. Wang, and H. Huang, *SciPost Phys.* **17**, 086 (2024).
- [31] N. Baù and A. Marrazzo, *Phys. Rev. B* **109**, 014206 (2024).
- [32] N. Baù and A. Marrazzo, *Phys. Rev. B* **110**, 054203 (2024).
- [33] L. Jezequel and P. Delplace, *SciPost Phys.* **18** (2025).
- [34] A. Y. Chaou, M. Moreno-Gonzalez, A. Altland, and P. W. Brouwer, *Phys. Rev. B* **112**, 035167 (2025).
- [35] R. J. Zijderveld, I. A. Day, and A. R. Akhmerov, *SciPost Phys.* **19**, 058 (2025).
- [36] A. Agarwala and V. B. Shenoy, *Phys. Rev. Lett.* **118**, 236402 (2017).
- [37] S. Mansha and Y. D. Chong, *Phys. Rev. B* **96**, 121405 (2017).
- [38] M. Xiao and S. Fan, *Phys. Rev. B* **96**, 100202 (2017).
- [39] N. P. Mitchell, L. M. Nash, D. Hexner, A. M. Turner, and W. T. M. Irvine, *Nat. Phys.* **14**, 380 (2018).
- [40] K. Pöyhönen, I. Sahlberg, A. Westström, and T. Ojanen, *Nat. Commun.* **9**, 2103 (2018).
- [41] E. Prodan, *Annales Henri Poincaré* **22**, 1133 (2021).
- [42] A. G. Grushin, Topological Phases of Amorphous Matter, in *Low-Temperature Thermal and Vibrational Properties of Disordered Solids*, edited by M. A. Ramos (World Scientific, 2022) Chap. 11, pp. 435–486.
- [43] A. Agarwala, V. Juričić, and B. Roy, *Phys. Rev. Research* **2** (2020).
- [44] B. Focassio, G. R. Schleder, M. Costa, A. Fazzio, and C. Lewenkopf, *2D Mater.* **8**, 025032 (2021).
- [45] J.-H. Wang, Y.-B. Yang, N. Dai, and Y. Xu, *Phys. Rev. Lett.* **126**, 206404 (2021).
- [46] H. Spring, A. Akhmerov, and D. Varjas, *SciPost Phys.* **11** (2021).
- [47] S. Manna and B. Roy, *Commun. Phys.* **6**, 10 (2023).
- [48] J. Ma and H. Huang, *Phys. Rev. B* **106**, 195150 (2022).
- [49] Q. Marsal, D. Varjas, and A. G. Grushin, *Phys. Rev. B* **107**, 045119 (2023).
- [50] S. Manna, S. K. Das, and B. Roy, *Phys. Rev. B* **109**, 174512

- (2024).
- [51] S. E. Skipetrov and P. Wulles, *Phys. Rev. A* **105**, 043514 (2022).
- [52] H. Spring, A. R. Akhmerov, and D. Varjas, *SciPost Phys.* **20**, 051 (2026).
- [53] A. G. Grushin and C. Repellin, *Phys. Rev. Lett.* **130**, 186702 (2023).
- [54] G. Cassella, P. d’Ornellas, T. Hodson, W. M. H. Natori, and J. Knolle, *Nat. Commun.* **14**, 6663 (2023).
- [55] P. Corbae, J. D. Hannukainen, Q. Marsal, D. Mu textasciitilde noz-Segovia, and A. G. Grushin, *Europhys. Lett.* **142**, 16001 (2023).
- [56] X. Cheng, T. Qu, L. Xiao, S. Jia, J. Chen, and L. Zhang, *Phys. Rev. B* **108**, L081110 (2023).
- [57] S. Franca and A. G. Grushin, *Phys. Rev. Mater.* **8**, L021201 (2024).
- [58] S. Bera, J. Dieplinger, and N. P. Nayak, *Phys. Rev. B* **109**, 174213 (2024).
- [59] M. F. Martínez, A. G. Grushin, and J. H. Bardarson, *Phys. Rev. B* **113**, 075417 (2026).
- [60] A. J. Uría-Álvarez and J. J. Palacios, *Phys. Rev. Res.* **7**, 043263 (2025).
- [61] Y. E. Kraus, Y. Lahini, Z. Ringel, M. Verbin, and O. Zilberberg, *Phys. Rev. Lett.* **109**, 106402 (2012).
- [62] D. T. Tran, A. Dauphin, N. Goldman, and P. Gaspard, *Phys. Rev. B* **91**, 085125 (2015).
- [63] M. A. Bandres, M. C. Rechtsman, and M. Segev, *Phys. Rev. X* **6**, 011016 (2016).
- [64] J.-N. Fuchs and J. Vidal, *Phys. Rev. B* **94**, 205437 (2016).
- [65] H. Huang and F. Liu, *Phys. Rev. B* **98**, 125130 (2018).
- [66] H. Huang and F. Liu, *Phys. Rev. Lett.* **121**, 126401 (2018).
- [67] J.-N. Fuchs, R. Mosseri, and J. Vidal, *Phys. Rev. B* **98**, 145 (2018).
- [68] D. Varjas, A. Lau, K. Pöyhönen, A. R. Akhmerov, D. I. Pikulin, and I. C. Fulga, *Phys. Rev. Lett.* **123** (2019).
- [69] R. Chen, D.-H. Xu, and B. Zhou, *Phys. Rev. B* **100**, 115311 (2019).
- [70] A.-L. He, L.-R. Ding, Y. Zhou, Y.-F. Wang, and C.-D. Gong, *Phys. Rev. B* **100**, 214109 (2019).
- [71] C. W. Duncan, S. Manna, and A. E. B. Nielsen, *Phys. Rev. B* **101**, 115413 (2020).
- [72] J. Fan and H. Huang, *Front. Phys.* **17**, 13203 (2021).
- [73] O. Zilberberg, *Opt. Mater. Express* **11**, 1143 (2021).
- [74] C.-B. Hua, Z.-R. Liu, T. Peng, R. Chen, D.-H. Xu, and B. Zhou, *Phys. Rev. B* **104**, 155304 (2021).
- [75] D. V. Else, S.-J. Huang, A. Prem, and A. Gromov, *Phys. Rev. X* **11**, 041051 (2021).
- [76] J. Jeon, M. J. Park, and S. Lee, *Phys. Rev. B* **105**, 045146 (2022).
- [77] J. Schirrmann, S. Franca, F. Flicker, and A. G. Grushin, *Phys. Rev. Lett.* **132**, 086402 (2024).
- [78] H. Roche Carrasco, J. Schirrmann, A. Mordret, and A. G. Grushin, *Phys. Rev. Lett.* **135**, 236603 (2025).
- [79] W. Caiger, F. Flicker, and M.-A. Sánchez-Martínez, *arXiv* 2602.02796 (2026).
- [80] R. J. Zijderfeld, A. Y. Chaou, I. A. Day, and A. R. Akhmerov, *arXiv* 2601.00784 (2026).
- [81] Y.-L. Tao, J.-H. Wang, and Y. Xu, *SciPost Phys.* **15** (2023).
- [82] J. Schirrmann, A. G. Grushin, and B. J. Wieder, *arXiv* 2512.19791 (2025).
- [83] K. Vynck, R. Pierrat, R. Carminati, L. S. Froufe-Pérez, F. Schef-fold, R. Sapienza, S. Vignolini, and J. J. Sáenz, *Rev. Mod. Phys.* **95**, 045003 (2023).
- [84] I. C. Fulga, F. Hassler, and A. R. Akhmerov, *Phys. Rev. B* **85**, 165409 (2012).
- [85] A. Shih, M. Casiulis, and S. Martiniani, *Phys. Rev. E* **110** (2024).
- [86] W. A. Benalcazar, B. A. Bernevig, and T. L. Hughes, *Science* **357**, 61 (2017).
- [87] W. A. Benalcazar, B. A. Bernevig, and T. L. Hughes, *Phys. Rev. B* **96**, 245115 (2017).
- [88] F. Schindler, A. M. Cook, M. G. Vergniory, Z. Wang, S. S. P. Parkin, B. A. Bernevig, and T. Neupert, *Sci. Adv.* **4**, eaat0346 (2018).
- [89] L. Trifunovic and P. W. Brouwer, *Phys. Rev. X* **9**, 011012 (2019).
- [90] J. Langbehn, Y. Peng, L. Trifunovic, F. von Oppen, and P. W. Brouwer, *Phys. Rev. Lett.* **119**, 246401 (2017).
- [91] M. Geier, L. Trifunovic, M. Hoskam, and P. W. Brouwer, *Phys. Rev. B* **97**, 205135 (2018).
- [92] S. Franca, J. van den Brink, and I. C. Fulga, *Phys. Rev. B* **98**, 201114 (2018).
- [93] B. Xie, H.-X. Wang, X. Zhang, P. Zhan, J.-H. Jiang, M. Lu, and Y. Chen, *Nat. Rev. Phys.* **3**, 520 (2021).
- [94] Compared to Ref. [68] we directly choose the superconducting pairing, Δ in Ref. [68], to be equal to the hopping t .
- [95] L. Fu and C. L. Kane, *Phys. Rev. B* **76**, 045302 (2007).
- [96] J. Kruthoff, J. de Boer, J. van Wezel, C. L. Kane, and R.-J. Slager, *Phys. Rev. X* **7**, 041069 (2017).
- [97] H. C. Po, A. Vishwanath, and H. Watanabe, *Nat. Commun.* **8**, 50 (2017).
- [98] E. Khalaf, H. C. Po, A. Vishwanath, and H. Watanabe, *Phys. Rev. X* **8**, 031070 (2018).
- [99] We note that we could have used these two methods with either of the particle-hole or chiral symmetries.
- [100] M. Sitte, A. Rosch, E. Altman, and L. Fritz, *Phys. Rev. Lett.* **108**, 126807 (2012).
- [101] L. Lu, J. D. Joannopoulos, and M. Soljačić, *Nat. Photonics* **8**, 821 (2014).
- [102] J. Schulz, J. Noh, W. A. Benalcazar, G. Bahl, and G. von Freymann, *Nat. Commun.* **13**, 6597 (2022).
- [103] S. N. Kempkes, M. R. Slot, S. E. Freeney, S. J. M. Zevenhuizen, D. Vanmaekelbergh, I. Swart, and C. M. Smith, *Nat. Phys.* **15**, 127 (2019).
- [104] Z. Wang, Y. Meng, B. Yan, D. Zhao, L. Yang, J. Chen, M. Cheng, T. Xiao, P. P. Shum, G.-G. Liu, Y. Yang, H. Chen, X. Xi, Z.-X. Zhu, B. Xie, and Z. Gao, *Nat. Commun.* **16**, 3122 (2025).
- [105] L. Gómez Paz, J. Schirrmann, A. Y. Chaou, I. Araya Day, and A. G. a. Grushin, *Topological gyromorphs* (2026).
- [106] C. W. Groth, M. Wimmer, A. R. Akhmerov, and X. Waintal, *New J. Phys.* **16**, 063065 (2014).

END MATTER

Appendix A: Symmetries of the model

The model introduced in the main text possesses time-reversal, particle–hole, and chiral symmetries. In addition, the effective Hamiltonian exhibits an average n –fold rotational symmetry, inherited from the structure of the underlying point set. In this Appendix, we present the explicit form of the corresponding symmetry operators for $n = 8$ and detail the transformation properties of both the real-space Hamiltonian and the effective Hamiltonian under these symmetries.

1. Particle-hole symmetry

The system’s particle-hole symmetry operator \mathcal{P} is

$$\mathcal{P} = \mathbb{1}_N \otimes \sigma_0 \otimes \tau_x, \quad (\text{A1})$$

where $\mathbb{1}_N$ denotes the identity matrix acting in position-space. Under particle-hole symmetry, the real-space Hamiltonian transforms as

$$\mathcal{H} = -\mathcal{P}\mathcal{H}^*\mathcal{P}^{-1}, \quad (\text{A2})$$

while the effective Hamiltonian transforms as

$$H_{\text{eff}}(\mathbf{k}) = -U_{\mathcal{P}}H_{\text{eff}}(-\mathbf{k})^*U_{\mathcal{P}}^{-1}, \quad (\text{A3})$$

where

$$U_{\mathcal{P}} = \sigma_x \otimes \tau_x. \quad (\text{A4})$$

2. Time-reversal symmetry

The model is also invariant under time-reversal symmetry. The corresponding operator \mathcal{T} is defined as:

$$\mathcal{T} = \mathbb{1}_N \otimes \sigma_x \otimes \tau_x, \quad (\text{A5})$$

where $\mathbb{1}_N$ denotes the identity matrix acting in position-space. Under this symmetry, the real-space Hamiltonian satisfies

$$\mathcal{H} = \mathcal{T}\mathcal{H}^*\mathcal{T}^{-1}, \quad (\text{A6})$$

and the effective Hamiltonian transforms as

$$H_{\text{eff}}(\mathbf{k}) = U_{\mathcal{T}}H_{\text{eff}}(-\mathbf{k})^*U_{\mathcal{T}}^{-1}, \quad (\text{A7})$$

where

$$U_{\mathcal{T}} = \sigma_x \otimes \tau_x. \quad (\text{A8})$$

3. Chiral symmetry

By combining the particle–hole symmetry operator Eq. (A1) and the time-reversal symmetry operator Eq. (A5), one can define a chiral symmetry operator given by

$$\mathcal{S} = \mathbb{1}_N \otimes \sigma_x \otimes \tau_0, \quad (\text{A9})$$

where $\mathbb{1}_N$ denotes the identity matrix acting in position-space. The Hamiltonian then satisfies

$$\mathcal{H} = -\mathcal{S}\mathcal{H}\mathcal{S}^{-1}. \quad (\text{A10})$$

The effective Hamiltonian transforms as

$$H_{\text{eff}}(\mathbf{k}) = -U_{\mathcal{S}}H_{\text{eff}}(\mathbf{k})U_{\mathcal{S}}^{-1}, \quad (\text{A11})$$

where

$$U_{\mathcal{S}} = \sigma_x \otimes \tau_0. \quad (\text{A12})$$

4. C_8M symmetry

Although the gyromorph possesses neither an exact global eightfold (C_8) rotational symmetry nor a mirror (M) symmetry, the effective Hamiltonian nonetheless inherits an approximate C_8M symmetry arising from the local eightfold symmetry of the underlying point configuration. The corresponding symmetry operator is given by

$$C_8M = \exp\left(-i\frac{\pi}{8}\sigma_0 \otimes \tau_z\right)\sigma_z \otimes \tau_0. \quad (\text{A13})$$

Under this symmetry, the effective Hamiltonian transforms as

$$H_{\text{eff}}(\mathbf{k}) = (C_8M) H_{\text{eff}}(R(\pi/4) \cdot \mathbf{k}) (C_8M)^{-1}, \quad (\text{A14})$$

where $R(\pi/4)$ denotes the two-dimensional rotation matrix corresponding to a counterclockwise rotation by an angle $\pi/4$, explicitly given by

$$R(\pi/4) = \begin{pmatrix} \cos(\pi/4) & -\sin(\pi/4) \\ \sin(\pi/4) & \cos(\pi/4) \end{pmatrix}. \quad (\text{A15})$$

Appendix B: Symmetry-Reduced Spectral Localizer

We start from the one-dimensional spectral localizer [12, 29], which can be written as

$$L(E, x) = s_y \otimes (\mathcal{H} - E) + \kappa s_x \otimes (X - x\mathbb{1}), \quad (\text{B1})$$

where s_i are Pauli matrices that act on an auxiliary subspace and $\mathbb{1}$ is shorthand notation for $\mathbb{1}_N \otimes \sigma_0 \otimes \tau_0$. For a system with even dimensionality, the spectrum of this operator, e.g. its half-signature, provides information about the topology of the system [12, 29]. In this case, L is off-diagonal and hermitian, which implies that its spectrum is symmetric around

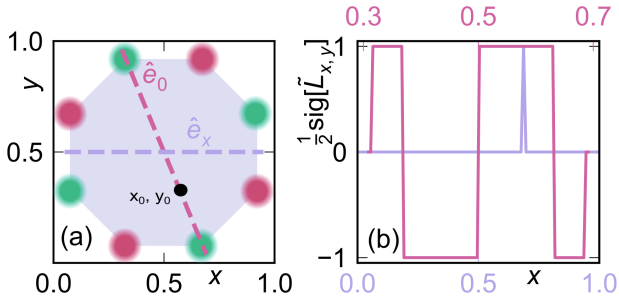


FIG. S1. (a) Chiral charges of the zero-energy modes for $\mu/t \sim -2$, green and red circles denote positive and negative chiral charges, respectively. The vector \hat{e}_d connects two opposite vertices of the octagon, while \hat{e}_x is the horizontal direction. We mark the point x_0, y_0 where we compute the invariant in Fig. 3(c) in the main text. (b) Half-signature of the symmetry-reduced localizer as a function of x , along direction \hat{e}_d in pink and \hat{e}_x in purple.

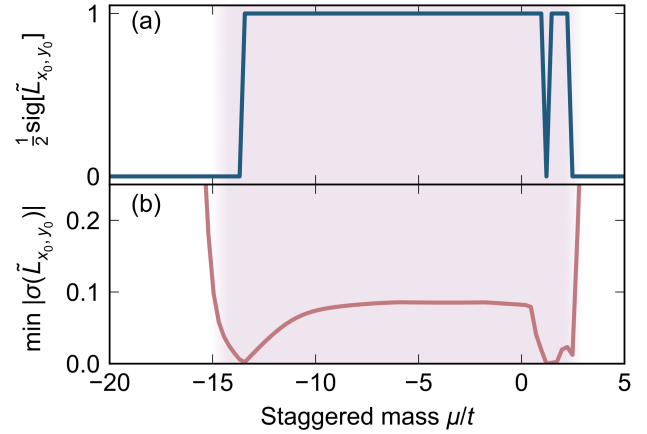


FIG. S2. (a) Half-signature of the symmetry-reduced localizer as a function of μ/t from Fig. 3(c), with $\kappa = 0.5$, $\mathbf{x} = (x_0, y_0)$. (b) Local gap of the symmetry-reduced localizer corresponding to panel (a) as a function of μ/t . The shaded region is that shown in Fig. 3.

zero energy, thus leading to a trivial signature. To overcome the implicit redundancy when defining an invariant, one can exploit the chiral symmetry of the Hamiltonian Eq. (1). Let $\mathcal{S} = \mathbb{1}_N \otimes \sigma_x \otimes \tau_0$ be the chiral operator, which satisfies

$$\mathcal{S}^\dagger = \mathcal{S}, \quad \mathcal{S}^2 = \mathbf{1}, \quad \{\mathcal{S}, \mathcal{H}\} = 0, \quad [\mathcal{S}, X] = 0. \quad (\text{B2})$$

If we apply a unitary transformation $\mathcal{U} = \begin{pmatrix} \mathcal{S} & 0 \\ 0 & \mathbb{1} \end{pmatrix}$ to the localizer in Eq. (B1), the relations in Eq. (B2) allow us to obtain a transformed localizer of the form

$$L_U(E, x) = \mathcal{U}^\dagger L(E, x) \mathcal{U} = \begin{pmatrix} 0 & \mathcal{S}[-i(\mathcal{H} - E) + \kappa(X - x\mathbb{1})] \\ [i(\mathcal{H} - E) + \kappa(X - x\mathbb{1})]\mathcal{S} & 0 \end{pmatrix}. \quad (\text{B3})$$

The advantage of this form is that its spectrum coincides with that of $L(E, x)$ while each of its off-diagonal blocks contains half of the spectrum, provided the blocks are Hermitian. This condition only holds for $E = 0$ as can be verified from the relations listed in Eq. (B2). Therefore, it suffices to consider only one block of $L_U(E, x)$ to extract the topological information of the system at $E = 0$, which defines the *symmetry-reduced localizer*

$$\tilde{L}_x = [i\mathcal{H} + \kappa(X - x\mathbb{1})]\mathcal{S}. \quad (\text{B4})$$

For a two-dimensional system as the one considered in this work, X can be replaced by any linear combination of the position operators X and Y such as $\hat{e}_d \cdot (\mathbf{X} - x\mathbb{1})$, with \hat{e}_d the direction along which we wish to project the system.

As discussed in the main text and Ref. [28], changes in the half-signature of this operator signal variations in the topological phase of the system. In Fig. S1, we show the half-

signature of the symmetry-reduced localizer as a function of x for $\mu/t \sim -2$, for which the system hosts eight zero-energy modes. We consider two different directions to evaluate the position operator: one choosing \hat{e}_d along \hat{e}_0 , connecting two opposite vertices of the octagon, and one choosing \hat{e}_d along the x -axis, \hat{e}_x , see Fig. S1(a).

Fig. S1(a) displays the chiral charges of the corner modes, colored with respect to the eigenvalues of the operator \mathcal{S} projected onto the zero-energy subspace. Variations in the half-signature occur precisely when the reference point x crosses a zero-energy mode, with magnitude determined by its chirality ± 1 . Hamiltonian eigenstates away from zero-energy do not contribute to the half-signature, as they come in pairs with opposite chiral charges. Consequently, \hat{e}_x , as well as any direction that projects pairs of modes with reversed chirality, fails to resolve the topology, whereas \hat{e}_0 successfully captures the changes in the half-signature [28, 29]. This argument underlies

our choice of \hat{e}_0 for computing the phase diagram in Fig. 3(c). The non-zero values observed along \hat{e}_x in Fig. S1(b) are due to small deviations from exact C_8 symmetry in the chiral charge distribution.

To assess the stability of the topological phase, it is helpful to analyze not only the half-signature of the symmetry-reduced localizer, but also its local gap, defined as the smallest absolute value of its spectrum [29], $\min|\sigma(\tilde{L}_x)|$. The size of the local gap sets a lower bound for the perturbation required to close the gap; only those perturbations whose magnitude is at least as large as the local gap can drive the localizer to change its signature, thereby altering the topological phase [29]. Hence,

a large non-vanishing local gap ensures that the half-signature is stable against perturbations, thus providing a robust phase.

In Fig. S2(a), we reproduce the localizer index, already shown in Fig. 3(c), and its corresponding local gap in panel (b). We observe that the gap remains open across the topological region, thereby confirming the stability of the phase. This plot also informs us that the numerical instability observed at $\mu/t \sim 0$ arises from the small real-space Hamiltonian gap at this region (see Fig. 1(c)), which is inherited by the localizer. In addition, the fact that the local gap remains finite also confirms that the chosen value of κ is suitable for capturing the phase transitions.